An ultrasound probe array for a high-pressure, high-temperature solid medium deformation apparatus

Citation: Ghaffari, H. O. and M. Pec. "An ultrasound probe array for a high-pressure, high-temperature solid medium deformation apparatus", Review of Scientific Instruments 91, 8 (August 2020): 085117. © 2020 Author(s)

As Published: http://dx.doi.org/10.1063/5.0004035

Publisher: AIP Publishing

Persistent URL: https://hdl.handle.net/1721.1/133169

Version: Author's final manuscript: final author's manuscript post peer review, without publisher's formatting or copy editing

An Ultrasound Probe Array for a High-Pressure, High-Temperature Solid Medium Deformation Apparatus

H.O.Ghaffari & M.Pec

MASSACHUSETTS INSTITUTE OF TECHNOLOGY, DEPARTMENT OF EARTH, ATMOSPHERIC AND PLANETARY SCIENCES,

CAMBRIDGE, MASSACHUSETTS, USA

Corresponding Author: mpec@mit.edu

Abstract- Inelastic deformation of minerals and rocks is associated with activation of various defects such as fractures, twins and dislocations. Active and passive ultrasound probes are potential tools to examine the nature of these defects under a broad range of pressure and temperature conditions. Here, we report on the development of an ultrasound probe array that allows us to monitor deforming samples in a high-pressure, high-temperature solid-medium apparatus (a modified Griggs rig). We utilize several broad-band miniature piezoelectric sensors that are placed above and below the sample to record acoustic emissions accompanying deformation and determine their locations in 1D. The emissions are recorded at 50 MS/s with a 12 bit resolution. Proper grounding and electric insulation of the sensors, together with optimized power delivery from the heating system, tremendously reduces electromagnetic interference (EMI) and allows for a background noise level of ≈90 mV at a full range of +/-2V and 60 dB amplification. The system is capable of recording acoustic waves from 80 kHz to 2.5 MHz at sample temperatures up to 1100˚C and confining pressure up to 2.5 GPa.

1. Introduction

Deformation of Earth materials is associated with activation of various defects which include fractures, grain and phase boundaries, twins, dislocations and point defects. It is the collective motion of these defects that makes deformation possible. In nature, deformation takes place over a vast pressure and temperature range, and therefore the relative contribution to strain by the individual types of defects changes with depth. Studying the processes occurring deep in the Earth and other planets experimentally requires achieving high-pressures (*HP*) and high-temperatures (*HT*) while the response of a sample (a single mineral or aggregation of minerals, i.e. a rock) is monitored by appropriate probes. Active and passive ultrasound probes are potential tools to examine deformation of materials under a broad range of *P-T* conditions. Such in-situ ultrasound probes are useful for establishing thermomechanical characteristics of the sample and for identifying the defect types contributing to strain at controlled external conditions such as pressure, temperature, stress, and chemical environment. Many fundamental questions in Earth science such as the nature of the "brittle-viscous" transition and the mechanisms of earthquake generation can be better constrained if data on the activity and *P-T* dependence of individual defects in various minerals and rocks is known.

To advance our understanding of these topics, we developed an ultrasound probe array that is integrated into a *HP-HT* deformation apparatus. Here we focus on a range of pressures between 0.3 to 2 GPa and temperatures between 100˚ to 1000˚C (corresponding roughly to 8 – 40 km depth). These conditions are typically covered by solid medium deformation apparatus such as the "Griggs" triaxial piston-cylinder rig. This apparatus type has been used extensively for understanding the mechanical behavior of rocks and minerals up to pressures of ≈3.5 GPa and temperatures of ≈1200˚C over the last ≈60 years (*Griggs, 1967, Tullis and Tullis 1986, Borch and Green 1989, Rybacki et al. 1998, Holyoke and Kronenberg 2010, Tarantola et al. 2012, Stewart et al. 2013, Burnley and Getting 2012*). Classically, two main observable mechanical parameters - displacements and forces - are monitored while as many other parameters as possible are held constant (i.e. pressure, temperature, fluid content, etc.). Monitoring of forces and displacements occurs externally to the pressure vessel and in a range of frequencies typically not higher than 0.1

kHz; this frequency range is fundamentally determined by the response time of the employed load cells and displacement transducers.

Mechanical data acquired during the experiments are coupled with post-mortem microstructural observations of the deformed samples and used to infer active deformation mechanism(s) in the sample at given experimental conditions. This approach yields precise measurements of long-term creep behavior of rocks and the accompanying microstructural record (e.g. *Hirth and Tullis 1994, Gleason and Tullis 1995, De Ronde et al. 2004, Heilbronner and Tullis 2006*, *Pec et al. 2012a, 2016, Holyoke et al. 2014, French et al. 2019*). However, relatively long response times of the load cells and displacement transducers and slow sampling rates mean that the data acquisition system (DAQ) will not capture fast, transient deformation. A number of processes can cause fast transient deformation in the kHz range and above during *HP-HT* experiments. Therefore, sampling over a broader frequency range could provide additional constrains on the active deformation mechanisms during an experiment. Due to the *HP-HT* conditions, placing probes on the sample is difficult, however buffer rods can be used to shield ultrasound sensors from the environment. Other monitoring methods suitable for *HP-HT* environments, such as using synchrotron radiation (*Burnley and Zhang 2008)*, low angle neutron scattering (*Kohlbrecher et al. 2007)* or laser (*Blacic and Hagman, 1977*) probes also have been reported.

In this paper, we describe our attempt to design and implement an array of ultrasound probes to study deformation behavior of samples at *HP-HT* conditions during the experiments. The organization of the paper is as follows: in Section 2 we briefly review the history of ultrasound probes in experimental geophysics, in Sections 3 and 4 we present a detailed description of our deformation apparatus installed at MIT, and then use analytical and numerical studies of synthetic wave propagation in the assembly to identify workable solutions. We also present temperature distribution measurements and calculations in order to determine the safe locations for the sensors. Section 5 describes miniature piezoelectric sensors we chose (and modified) for our ultrasound array, together with the sensor's characteristics. Section 6 describes our methods to reduce the electromagnetic interference (EMI) level in order to increase the signal to noise ratio and record signals as weak as possible. In the last section, we demonstrate the capabilities of the developed system using experiments on quartzites and arrays of 2 to 4 sensors described in section 5.

2. Brief History of Ultrasound Surveying in Experimental Geophysics

Laboratory studies of the propagation of sound waves through minerals and rocks at high hydrostatic pressures and later, also high temperatures were pioneered in the 20th century by Percy Bridgman and Francis Birch and played a crucial role in enabling scientists to interpret seismic data (*Bridgnam,1931; Birch,1939*). Variation of longitudinal (P) or transverse (S) wave velocity with increasing pressure, temperature and rock type can be used to explore processes responsible for the observed discontinuous variations in velocity in Earth's interior (*Kern 1982*). Such anomalies in sound velocities have been established in the global seismic models and are thought to correspond to lithological boundaries and phase transitions (*Li and Liebermann 2014*). A number of methods were developed such as *pulse-transmission* and *pulse-echo* methods to measure the wave velocities and extract data at ever increasing pressures and temperatures (the interested reader is referred to excellent reviews by *Li and Liebermann 2014* and *Bass and Zhang 2015* for a summary of ultrasonic techniques in hydrostatic experiments).

With the development in instrumentation, measuring of wave velocities during non-hydrostatic, rock deformation experiments became possible. In deformation experiments, the wave velocity evolution is used as a proxy for damage since deformation induces defects in the rock which slow down the propagation velocity of sound waves (*Schubnel and Guéguen, 2003*) This class of laboratory experiments can be summarized as "active" experiments where a known pulse is generated and is recorded later, after it propagates through the sample. The travel time and the difference in amplitude and spectra between the generated and recorded signals contain information about the sample microstructure.

In parallel to the measurements of wave velocities in rocks and minerals, metallurgists and engineers were developing methods to study noises accompanying deformation of various materials in order to predict failure. These noises are currently known under the term "acoustic emissions" (AEs) and provide fundamental insight into the processes which accommodate inelastic strain *(Agarwal et al.,1970; Wadley and Mehrabian ,1984; Lockner et al.,1993, Benson et al,2008; Thompson et al.,2009, Vingordov ,2010; Ghaffari and Young, 2013, Ghaffari et al. 2019*). AEs are primarily caused by the nucleation and propagation of cracks. However, other processes such as twinning nucleation (*Vinogradov et al.,* 2016), avalanche-like propagation of dislocations (*Weiss and Marsan,2003*) and structural phase transitions (*Glover et al.,1995*) in

rocks (and other materials) undergoing straining are also accompanied by acoustic emissions. This class of laboratory experiments can be summarized as "passive" experiments where noises generated by the sample during deformation are recorded by a net of sensors. A vast number of Earth science studies exploits AEs at low pressures (typically < 200 MPa) and low temperatures (typically < 100˚C) where tens of contact-based probes can be mounted directly to large samples to constrain fracture and friction of rocks (*Lockner et al.,1993; Passelègue et al.,2013; McLaskey and Kilgore,2013; Thompson et al.,2009; Benson et al.,2008*; *Ghaffari et al.,2014*). The characteristics of AEs share a number of similarities with crustal earthquakes suggesting that similar processes operate in both, although on vastly different time and length-scales. This assumption is rooted in a general scaling law which states that dominant frequencies of earthquakes scale inversely with source dimension (*Aki and Richards,2002*). Both natural earthquakes as well as AEs obey the Gutenberg-Richter law (*Gutenberg and Richter 1955, Bak and Tang 1989*) and therefore it is inferred that similar physical process operate in both. Source location, focal mechanisms and other standard seismological techniques can be applied to AEs as well to gain insight into the physical processes that generated the recorded signals provided sufficient spatial coverage of the sample by sensors exists.

"Active" and "passive" experiments can be summarized as "laboratory seismology". Constant development in sensor sensitivity and miniaturization together with the increase of storage capacity and processing power of computers, and new methods of data analysis (*Rouet-Leduc et al. 2017*) have made "laboratory seismology" a powerful tool of scientific inquiry. Recent developments in rock deformation and ultrasound instrumentation – especially the integration of ultrasound probes to a D-DIA apparatus installed at the Advanced Photon Source synchrotron in Chicago (*Schubnel et al. 2013, Wang et al. 2017*) – have allowed for the expansion of the pressure - temperature space at which "laboratory seismology" is feasible and lead to new insights into intermediate-depth and deep earthquakes (*Tingle et al.,1993; Dobson and Meredith,2002; Schubnel et al. 2013, Gasc et al. 2011, Incel et al. 2017, Wang et al. 2017*), as well as into the influence of melting on acoustic wave propagation in mantle lithologies (*Chantel et al. 2016*). The D-DIA apparatus can reach high pressures between 1 - 15 GPa (*Wang et al. 2003*), however it can deform only very small samples (2-mm diameter and 3-mm long) and requires synchrotron x-ray radiation to measure stress and strain. Hence there is room for integrating ultrasound probes into a rock deformation apparatus capable of deforming larger

samples at *HP-HT* conditions that does not need expensive synchrotron radiation to acquire mechanical data; the Griggs rig.

Early attempts to record AEs at *HP-HT* conditions in a Griggs rig used an ingenious wide-band optical measuring system (*Blacic and Hagman 1977*). While the initial results looked promising, no further development of this system was pursued. Later attempts to collect AE data at *HP-HT* conditions were performed in a modified Griggs rig using piezoelectric sensors placed on the base plate (*Green et al. 1992, Tingle et al. 1993, Okazaki and Hirth 2016*). Such sensor position allows counting of AE as a function of time and correlating these data with the mechanical and microstructural record. However, with only one sensor employed, source locations cannot be determined. Recently, a next generation of the Griggs rig has been designed and built by Sanchez Technologies with the specific task to make integration of ultrasound sensors above and below the sample possible (*Schubnel et al. 2015, Précigout et al. 2018*). This sensor geometry allows for performing *pulse-transmission* experiments as well as basic AE location. The current design is an iteration on the solid medium deformation apparatus designs (*Griggs, 1967, Tullis and Tullis 1986, Tingle et al. 1993, Rybacki et al. 1998*) and is described in further detail below.

3. Solid medium deformation apparatus: loading mechanism, sensor set-up and temperature distribution

In this section we briefly describe the workings of the solid medium piston-cylinder deformation apparatus and discuss the challenges in combining the apparatus with an ultrasound array system. Any modifications in the apparatus to accommodate the ultrasound sensors must consider the mechanical stability of different parts of the apparatus. The ultrasound sensors have a limited resistance to high temperature, high pressure and induced electromagnetic noises making the integration of the two systems challenging.

3.1 *The Sanchez Technologies Deformation Apparatus*

A schematic of the apparatus is shown in **Figure 1**. The apparatus consists of 1) the press frame with hydraulic cylinders driving the σ_1, σ_3 and pre-stress rams, 2) syringe pumps driving the confining and axial rams, 3) DAQ and control unit, 4) pressure vessel, base plate, σ_1, σ_3 and pre-stress pistons, 5) cooling system 6) heating system. The current "Sanchez" apparatus is a next

generation design of the "Griggs" apparatus. The main focus of this paper is on the ultrasound probe array; thus, we describe, only the necessary basics of the solid medium deformation apparatus and the interested reader is referred to *Rybacki et al. 1998* for a more detailed description of the predecessor to the current design.

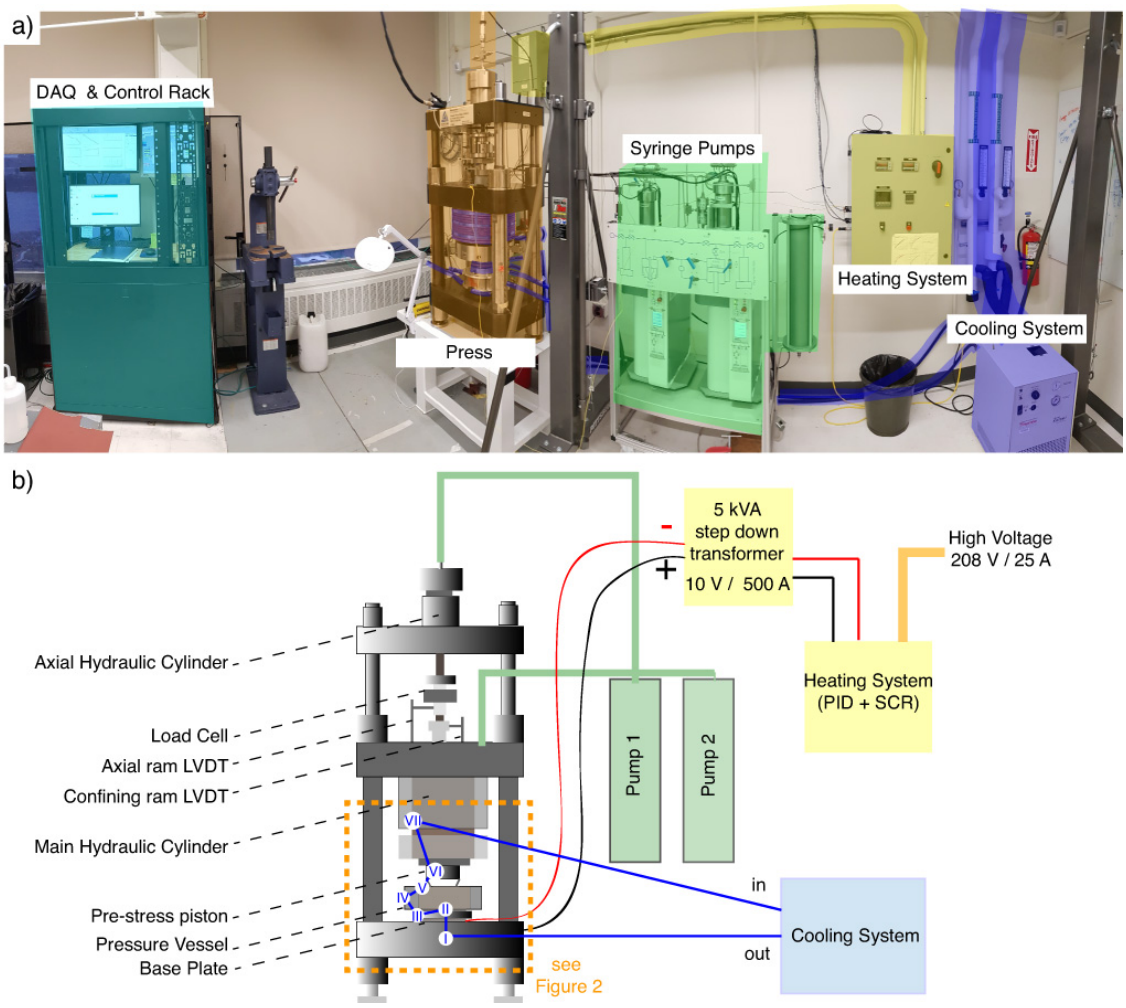

Figure 1. The solid medium deformation apparatus and its components. a) A panoramic view of the installed apparatus. Individual systems are color-coded. b) A schematic drawing of the apparatus and its main components. Roman numerals indicate the path of the cooling water through the apparatus. Systems in orange dashed rectangle are shown in Figure 2 in more detail.

3.1.1 *The Press and Syringe Pumps*

The press frame is formed by four vertical tie-bars that hold three horizontal platens. The main hydraulic cylinder drives confining pressure and pre-stress rams. It is attached to the middle platen and is driven by a high precision 100 ml syringe oil pump (Sanchez STIGMA 100) that can reach

pressures of up to 150 MPa. This oil pressure corresponds to a force of ~1430kN exerted by the confining pressure ram. The axial hydraulic cylinder is placed on the top platen and is driven by a second 1000 ml syringe pump (Sanchez STIGMA 1000) that can reach pressures of up to 30 MPa which corresponds to a load of about 230 kN on the axial piston. Each syringe pump has a pressure gauge (HBM-P3ICP) to measure the oil pressure inside the pump. The axial piston is composed of a tungsten carbide actuator (WC with 15% Cobalt binder) and steel (CPM-M4) piston and has a 1.5 mm hole with an outlet above the middle platen for threading wires.

3.1.2 *DAQ and control unit*

Load on the σ_1 piston is recorded by an external load cell (HBM C2 – 200 kN), and is further monitored by a pressure gauge (Keller PAA-33X) measuring the oil pressure in the axial ram. Confining pressure is monitored by a pressure gauge (HBM-P3ICP) recording the oil pressure in the confining ram. Displacement of the σ_1 and σ_3 pistons is monitored by Linear Variable Differential Transformers (LVDTs) that are mounted externally between the top and middle platen (Figure 2). The LVDT recording the σ_1 piston position has a range of 50 mm (HBM – WA-50) and the LVDT monitoring the confining pressure ram position has a range of 20 mm (HBM – WAB-20), both of the LVDTs have an accuracy of $\approx$2 μm. The temperature at the control thermocouple as well as the volts and amperes in the secondary circuit of the step-down transformer (more details in Section 3.1.5) are recorded together with the room temperature. All these data are typically logged at a rate of 1 sample / second using an 8 channel DAQ system (QuantumX Data Acquisition System, maximum sampling rate per channel 40 kS/s); dynamic experiments can be recorded at a rate of several hundred samples per second, however the noisiness of the data increases.

3.1.3 *Pressure vessel and pistons*

The confining and axial rams are each in contact with independent pistons made of tungsten carbide (manufactured by Dura-metal Products Co., WC with 15% cobalt binder) that transmit forces to the sample assembly within a pressure vessel (**Figure 2**). The pressure vessels have a bore diameter of 25.4 mm (1 inch) and consist of a tungsten carbide core surrounded by steel rings and a cooling ring on the outside of the vessel. The current pressure vessels (Max

Voggenreiter GmbH) can achieve confining pressures of up to 2 GPa. The maximal force exerted by the confining pressure ram can generate pressures of 2.8 GPa in a pressure vessel with a 25.4 mm bore.

3.1.4 *Sample assembly*

In **Figure 2** we show a schematic of the sample assembly. The main principle of load distribution is as follows: the sample is placed between alumina pistons and these pistons transfer the load to the sample from the hydraulically driven axial ram. The confining pressure is achieved by the collapse of the solid medium, i.e., cylinders of salt, which transfer the confining pressure from the σ_3 piston and the confining pressure ram to the sample through action – reaction principle. The salt sleeves are in contact with a lead disk on top of the assembly which evenly transfers the load from the σ_3 piston. The graphite furnace (**Figure 2**) encapsulates the sample and parts of the alumina pistons. The sample can be heated to the melting point of the confining medium (up to ≈1100°C at 2 GPa with NaCl salt).

3.1.5 *Heating*

Electrical power is transferred to heat through graphite‘s electrical resistance i.e., Joule heating process. The amount of supplied power is controlled by a proportional-integral-derivative (PID) controller (Eurotherm 3504) connected to a *s*- or *k*- type thermocouple touching the center of the sample. The PID controller communicates with a silicon-controlled rectifier (SCR) to tame the alternating current (AC) and deliver the desired amount of power to the furnace. We use a ControlConcepts microFusion SCR which can fire in fast zero-cross firing mode which cuts AC at zero voltage and avoids high-frequency noise peaks associated with phase-angle firing (see detailed discussion in Section 6). Minor temperature fluctuations are observed at low output % due to the increased minimal quantum of energy compared to phase angle firing, however this problem disappears at higher output % where the temperature is held as steady as during phase angle firing. Safety features include a magnetic flow meter to monitor the rate of the cooling water flow and an additional thermocouple placed in the sensor or thermocouple cavities at the base plate set to turn of the heating if the temperature crosses a set threshold (**Figure 3**).

3.1.6 *Cooling*

Cold (≈15˚C) water is circulated by a Thermo Scientific Neslab I cooling system. The cold water path is such that it is first introduced inside the base plug following to the outer radius of the base plate, into a cavity inside the base plate close to the bottom of the sample assembly where the sensor array is located. Subsequently, the water travels on the outside diameter of the pressure vessel, into a cooling ring located on the top of the pressure vessel and around the pre-stress piston. Finally, the water cools the hydraulic ram before returning to the heat exchanger as shown in Figure 2 in detail.

3.2 *Ultrasound Probe Array*

There are several problems in recording AEs in a Griggs-type apparatus: 1) induced electromagnetic interference noises due to joule heating process mask low amplitude AEs. With increasing temperature the amplitude of the acoustic signals typically decreases; weak signals are potentially dominant during creep deformation. Therefore, acquisition of signals with high ratio of signal to noise is critically important during *HP-HT* experiments. 2) Samples must be in the vicinity of a hot furnace for a long time. The exact distribution of temperature in the apparatus dictates the locations where sensors can be placed as most contact-based probes will not tolerate high temperatures for long term. Efficient cooling of the sensors to maintain the temperature in a tolerable range is essential. This will be dependent on the type of piezo-element and assembly of the sensors. 3) The ultrasound probes have to be mounted on buffer rods which should be good acoustic conductors and good thermal insulators, additional interfaces and travel length from source to receiver leads to signal attenuation. 4) The size of the samples is small, varying from tens of millimeters to hundreds of micrometers in length and diameter; a "typical" Griggs sample for co-axial deformation is 12 mm long and 6.3 mm diameter; a sample for general shear deformation is only 0.5 – 2 mm thick. 5) The loading geometry allows the placement of sensors only along the loading axis limiting spatial coverage of the sample.

3.2.1 *Upper Ultrasound Probe Array*

As shown in **Figures 1** to **3** we can place a number of piezoelectric sensors above and below the sample. We have split the upper σ_1 piston into two pieces, a lower 60 mm long, 8 mm

outer diameter piston serves as a spacer to position the piezoelectric array in a low temperature zone safe for the sensors.

The upper σ_1 piston is 40 mm long, 8 mm diameter with an increased diameter of 12 mm at the top where it makes contact with the σ_1 actuator. Two different upper σ_1 piston were made for specific sensor geometries; one has three ≈1.6 mm diameter cavities where miniature sensors can be inserted (**Figure 3**), another one has a central 4 mm diameter cavity for placing of a larger, ~2.5 mm diameter miniature sensor with proper EMI shielding. The small cavity sizes assure that the structural integrity of the piston, which can bear a load of up to 230 kN, is not significantly compromised. Our miniature sensors transmit the signal through 0.3 mm diameter 50-ohm impedance BNC wire and are spring loaded against the σ_1 actuator to assure good coupling. Multiple 0.3 mm thick wires can be threaded through the σ_1 actuator hole.

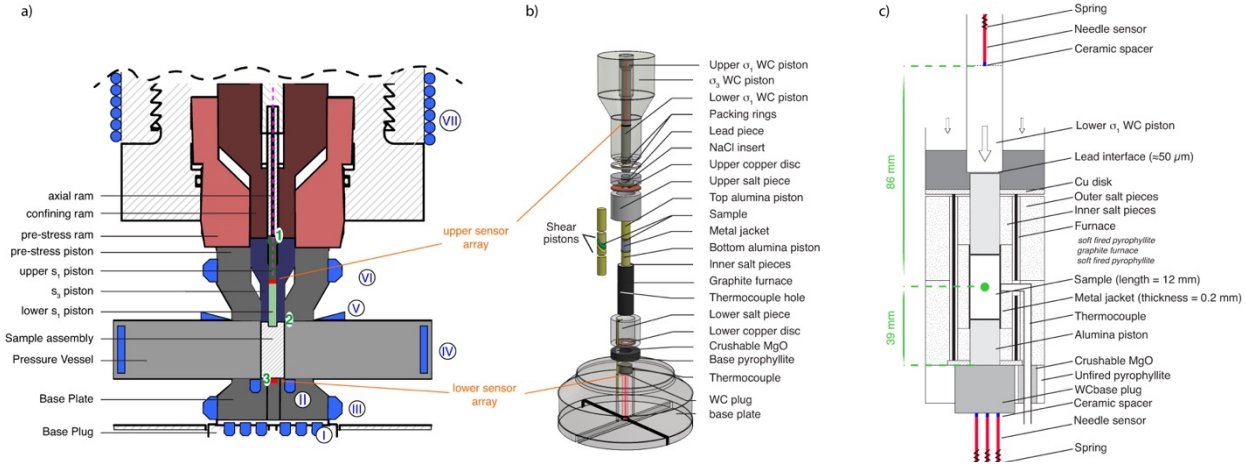

Figure 2| Schematic of the loading rams & pistons and the sample assembly. a) Detailed schematic of the loading rams & pistons. Position of the ultrasound sensor arrays is highlighted in red. Blue roman numerals show the cooling water path. Purple dashed line shows the position of the ø = 1.5 mm central hole for threading wires in the σ_1 loading ram and piston. Green Arabic numerals show positions of thermocouples for measurements reported in Figure 4 b) exploded-view of the sample assembly, WC pistons and base plate. Sensor locations are shown with red lines (modified after *Précigout et al. 2018*). c) detailed schematic of the sample assembly at hit-point. The distances from the center of the sample to the lower and upper sensor array are shown in green (modified after *Pec et al. 2012b*).

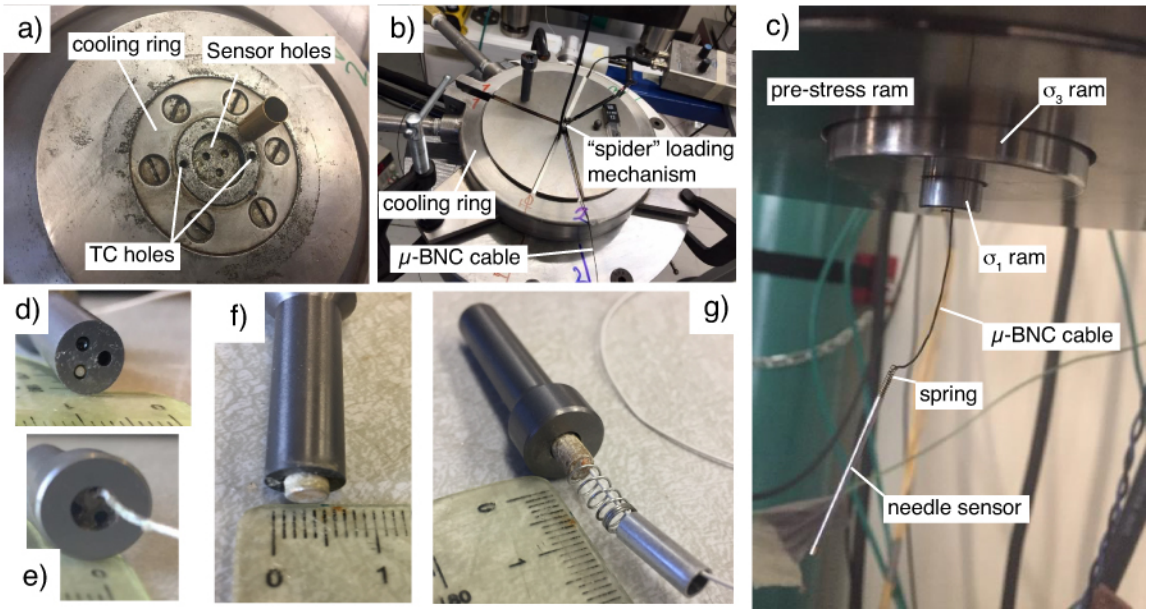

Figure 3 Images of the sensor housing. a) Base plate with 3 cavities arranged in a triangular pattern to mount piezoelectric sensors. The side holes are for thermocouples (TC). A hollow gold jacket is shown as the scale (ø=6.7mm; h~13). b) View from the back of the base plate (i.e. other side than shown in (a)). We employ three miniature needle sensors, each with its dedicated groove for threading the micro-BNC cables. The springs of the sensors are placed against a screw-mounted "spider" loading mechanism. The spider is made of plastic to assure good electric insulation. c) view of the top senor position. d - e) Views from the bottom and top of the upper σ_1 piston with three cavities. One of the cavities is filled with a miniature needle sensor. The micro-BNC cable is used to thread easily the wire through the axial ram. f - g) upper σ_1 piston with one larger hole to accommodate larger diameter needle sensor. CAD drawings of the base plate and pistons are available for download from *Ghaffari and Pec 2020.*

3.2.2 Lower Ultrasound Probe Array

The lower piezoelectric array is not as space-constrained as the upper piezoelectric array and can be cooled much more efficiently due to the fact that no moving parts are present (**Figures 2** and **3**). Since the base plate supports both the load from the confining pressure ram as well as the σ_1 ram during deformation, the placement of sensors must not compromise its mechanical stability. The design shown in Figure 3a & b was successfully tested up to 1 GPa confining pressure.

3.3 ***Temperature Distribution in the Apparatus***

To define a minimum "safe zone" for placement of the sensors, we have characterized the temperature distribution in the base plate and on the top of the pressure vessel and σ_1 actuator in a series of calibration experiments (**Figure 4**). We can modulate the temperature at which the sensors are located by placing ceramic spacers of varying thickness between the sensors and the WC plug (See **Figure 2c**). Piezoelectric crystals deteriorate if used above about half of their Curie

temperature (350°C for PZT-5A and 1150°C for LiNb); the epoxy which embeds the crystals and the connecting wires usually deteriorates at temperatures of about 100˚C. Our measurements document that for a sample temperature of 750˚C, moving about ~4 mm away from the WC plug using an alumina spacer with the current cooling design results in a tolerable sensor temperature of about ~90˚C. Moving from the WC plug further away to ~7 mm allows sample temperatures of ~1000˚C in the sample. The attenuation in a good sound conductor such as alumina ($V_p \approx 9.9$ km/s, thermal conductivity = 18 W m^{-1} K^{-1}) or zirconia (Vp ≈ 4.6 km/s, thermal conductivity = 5 W m^{-1} K^{-1}) ceramic should not suppress ultrasound waves significantly over these distances. A least-squares linear fit to the measured data set yields: $T_{pzt} \cong \alpha(d)T_S + T_0$ in which $T_{pzt}$and T_S are temperatures in the piezoelectric sensor and in the center of the sample, respectively; $\alpha(d)$ is the variable slope which depends on the alumina spacer thickness given by $\alpha(d) \cong (8.13 + 0.76d)^{-1}$ with d as the thickness of alumina spacer and T_0 is the y-intercept (≈23 ˚C). Recasting the above relation for a constant temperature of the piezoelement (T_{pzt}), we obtain an approximated minimum thickness of the spacer: $d \geq (\frac{1.31 \times T_S}{(T_{pzt} - T_0)} - 9.7)$ for d in millimeters that is needed to keep the sensor at the desired temperature (**Fig.4**).

Figure 4. Temperature distribution in the apparatus. a) temperature at the base plate (#3 in Figure 2). Three independent experimental measurements with different thickness of alumina spacers (black symbols). Contours show calculated T distribution based on spacer thickness. For a sample temperature of 800˚C and a desired temperature of <80˚C in sensor zone yields ~10mm spacer thickness. b) temperature at the top of the σ_1 ram (#1 in Figure 2) and top of the pressure vessel (PV, #2 in Figure 2).

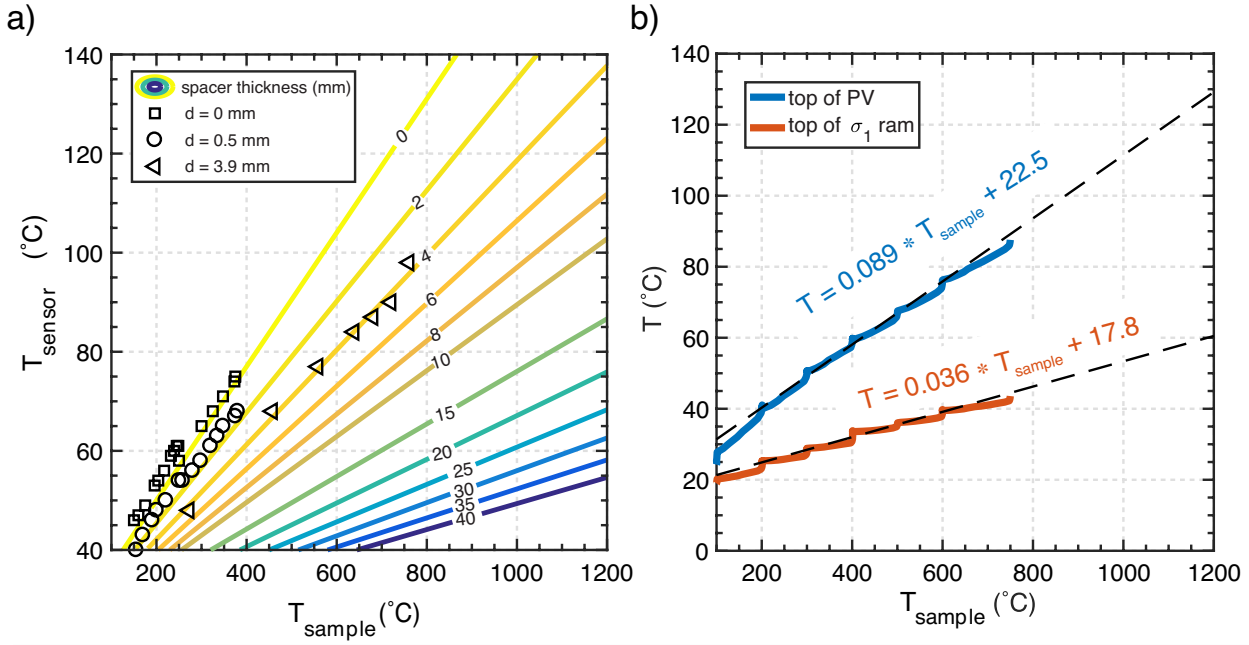

Cooling of the upper piezoelectric array is not as efficient as for the lower array, because cooling water circulates around the pre-stress piston which is not in direct contact with the σ_3 or σ_1 tungsten carbide pistons. Cooling of the main hydraulic ram provides a significant heat sink; however, the ram is relatively far away from the σ_3 or σ_1 tungsten carbide pistons for efficient cooling (**Figure 2a**).

4 Acoustic wave propagation in the solid medium deformation apparatus

To optimize the sensor array, we have conducted analytical and numerical modelling to gain further insights into wave propagation in the deformation apparatus. The center of a standard 12 mm long sample is 39 mm away from the lower piezoelectric sensor array and 86 mm away from the upper piezoelectric sensor array at the hit-point. The use of ceramic spacers to position the sensors at an appropriate temperature as described in Section 3.3 adds another 1 – 10 mm distance between the sensors and the sample. For a sensor at top and bottom, in an idealized case without refraction of waves on interior boundaries, the arrival at the top sensor array is delayed by ≈10 μs compared to the bottom sensor-array allowing for confident source location along the long sample axis (Z-axis).

We further performed numerical simulations of wave propagation from an impulsive source using the acoustic module of COMSOL Multiphysics finite element code in a simplified 2D set-up with soft boundaries (i.e. energy gets absorbed by confining salt- **Fig.6**). We used several scenarios varying the source-time function and its spatial location to study possible effects of both parameters, i.e., impulsiveness and source locations, on the recorded signals. In **Fig.6**, we show a derivative Gaussian impulse function of ~ 2μs duration with source location close to the lower right hand sample boundary. The model takes into account the refraction effects due to material discontinuity at interior boundaries. The simulation also includes effects of acoustic impedance contrasts which affect partition of ray energy among reflected and refracted rays (COMSOL 3.5 Manual).

Without considering mechanical stability of base plate, we monitor the waveforms along 5 sensor-points arranged in a row in 2D (**Fig.6a**). The time difference in P-wave arrival at the bottom sensor array between sensors spaced at ≈6 mm is ≈350 ns, i.e., about 17-35 times the time resolution if recording at rates of 50 – 100 MS/s.

From our calculations and numerical simulations, locating the AE source in 1D is possible.

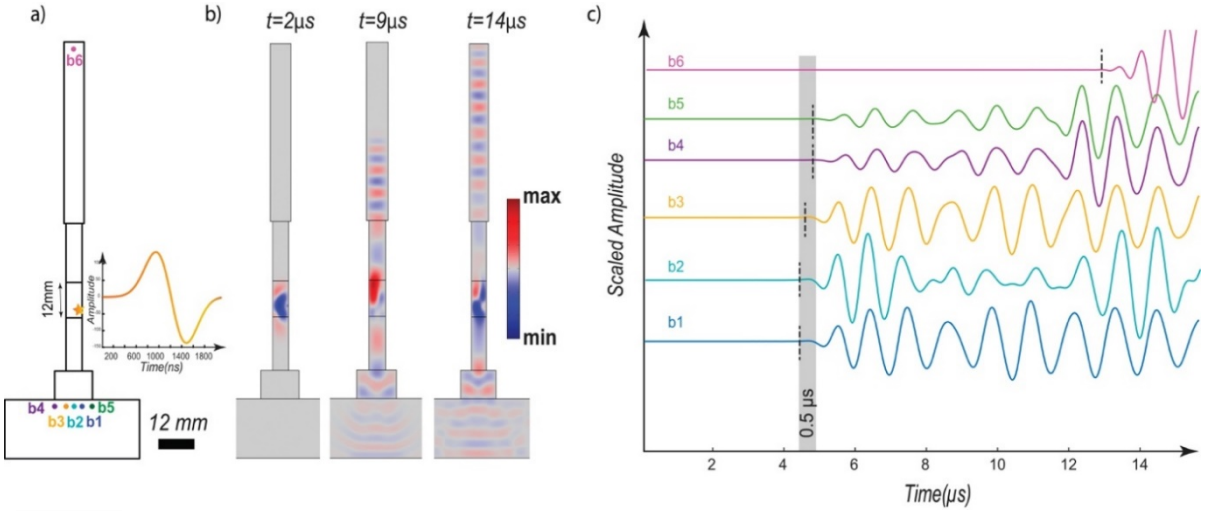

Figure 6| Numerical model of elastic P-wave propagation in the sample assembly. The velocity in the sample, alumina pistons, WC and steel was set to 6 km/s, 9.9 km/s, 6.7 km/s and 5.9 km/s respectively. a) model geometry. Sample size is 6.35 mm in diameter and 12 mm in length. Spacing between the sensors b1 – b2 and b2 –b3 is 3mm, b4 and b5 are 4.5 mm away from the last sensor to their right (or left). An impulsive source with a duration of 2μs occurs at the bottom right of the sample (Yellow star). b) wave field in different time intervals. c) waves recorded at individual stations (see a) for position of sensors). Sampling resolution is set to 20 ns i.e. 50 MS/s.

5 Miniature Piezoelectric Sensors, Amplifiers and DAQ system

To design the optimal ultrasound recording system for our *HP-HT* apparatus, we need to decide on a frequency band in which the majority of ultrasound excitations are expected for passive ultrasound experiments.

5.1 Passive Probes

Having previous knowledge of the sources (range of magnitudes and frequencies of excitations) is helpful to restrict the desired band. A wealth of data from ultrasound experiments on large rock samples under low confining pressures provide some clues on the frequency range of emitted waves (from 10s of kHz to ~1 MHz). Given the scaling between source dimensions and frequency (*Aki and Richards 2002)* we would generally expect higher frequency sources to be dominant in smaller, high pressure experiments. Furthermore, the process by which AE are generated under *HP-HT* might be more complex than fracture- and friction-dominated signals from low confining pressure experiments. These processes could yield a broad range of frequencies or mixed frequencies of vibrations. Unfortunately, ultrasonic data and related knowledge of defect dynamics from *HP-HT* experiments is currently very limited. The few rock-

deformation studies under *HP-HT* conditions which used ultrasonic sensors to study AEs in the D-DIA on even smaller samples than used in the Griggs employed piezoelectric sensors with a resonance frequency of 2-4 MHz (e.g. *Schubnel et al,2013*)

Due to the temperature constraints described in Section 3.3, the sensors are not in direct contact with the sample and sound waves must travel through alumina rods and WC plugs or pistons as well as a thin layer of gold. In the case of the top sensor, there is also a thin lead interface (Figure 2c). Such additional interfaces dissipate the energy of emitted waves and attenuate weak waveforms as well as waveforms with a high frequency.

5.2 Sensors, Amplifiers & DAQ

Considering the above-discussed points and restrictions in mounting multiple ultrasound probes, we opt to use broad-band miniature needle-like sensors with a resonance frequency of 2.5 MHz with different lengths but a fixed diameter of about 1.5 mm (**Fig.7**). The needle is composed of a metallic or brass jacket which includes insulating layers, conducting wire, back-up element and a miniature 0.5 mm diameter piezoelectric PZT- 5A crystal. The length of needles can be adjusted from ~5 mm to ~4 cm which allows us to place the sensors into a zone of appropriate temperature using ceramic spacers coupled to the tip of the needle. The needles are spring-loaded (**Fig.2a**; **Fig.7b**) allowing for controlled coupling of the element with the WC plugs and pistons. The small diameter allows us to place multiple sensors into the space-constrained apparatus with minimal compromise of mechanical integrity of the individual parts housing the sensors. To achieve high electrical conduction and high sensor sensitivity, a conductive coat (*gold, silver or CuNi*) is used before each test. To reduce the EMI effect, we spray an electrical insulator layer (CRC Urethane Seal Coat Viscous Liquid Coating) on the sensor and subsequently jacket the sensor in a thin non-conductive tube such as PTFE (**Figure 7**). In addition to this extensive electrical insulation of the sensors themselves, the interior of the sensor cavities are also covered by a thin dielectric insulator layer applied by spraying. The piezoelectric sensor has to be completely electrically isolated from the base plate or the WC piston in order to minimize EMI noises.

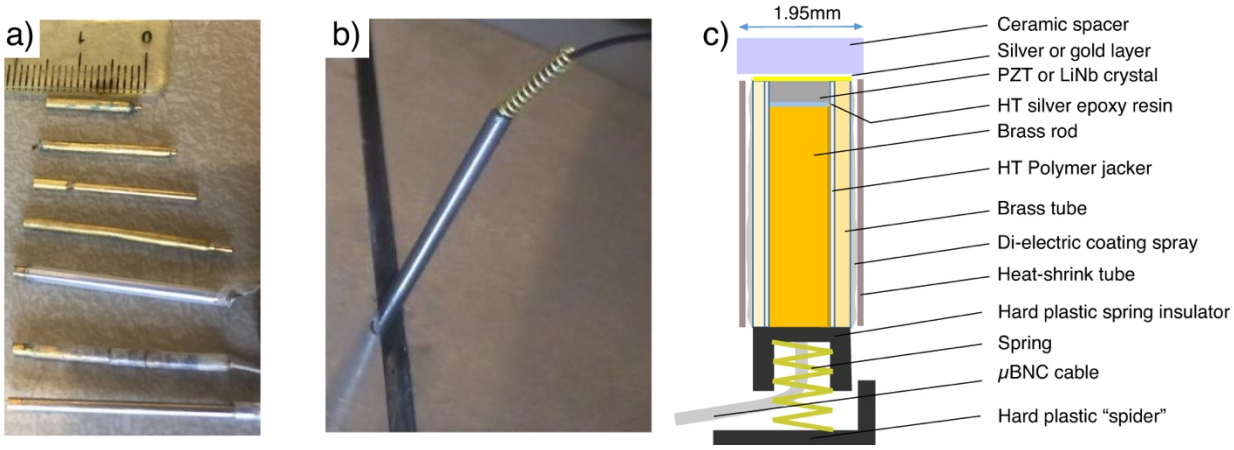

Figure 7| (a) Miniature needle-sensors of different lengths and an embedded piezoelectric element with the size of ~0.5 mm or 1 mm. The sensor lengths vary from 13 mm to 33 mm. Shorter needles are used for higher temperatures (>500˚C) in combination with longer alumina or zirconium oxide spacers to avoid high temperatures in the vicinity of the sensor. Alternatively, one can use LiNb piezoelectric crystals with high temperature epoxy. Bottom: spring loading mechanism is employed to achieve high stability coupling mechanism. c) shows internal design of a brass-based needle with silver (or gold) vapor deposit.

To characterize the (relative) response of our sensors and amplifiers, we use a wave generator to pulse signals of different shape and frequency. The output signal is split into two sub-signals; one visualized in oscilloscope (or DAQ) system and another triggers a piezoelectric sensor (as a reference source) where the electrical charge is converted to mechanical oscillation. The reference source is attached face-to-face to another sensor along a thin glass or mica interface to ensure the receiving sensor is not triggered with electromagnetic interference noise (**Figure 8**). We generate electrical sinusoidal pulses with an amplitude of 5V and duration of 5μs where the frequency changes from 5 kHz to 15MHz. We use a broadband amplifier (Itasca Co.) sensitive from 50 kHz up to 15MHz. Data are collected using a 4-channel USB oscilloscope recording at 50 MS/s and a 12bit resolution (TiePie HS4-50). Using these amplifiers,
amplification by 60 dB is almost flat for the source in the frequency range from 50 kHz to 1.5 MHz. Frequencies from 1.5MHz to 15MHz are amplified nonlinearly in a way that amplification decreases exponentially from 52dB to 37 dB as the frequency increases. **Figure 8c** shows that the response of one of the sensors is almost flat to generated waves in the range of 600 kHz to 2MHz and a clear resonance peak occurs around 2.5MHz. We define a parameter called sensitivity which is a logarithmic measure of the amplitude of the waves in receiver sensor relative to the generated waves and plot it in **Figure 8c**. Note that the received signal's amplitude and shape will be

affected by the quality of coupling with the WC plug as well as the length of the alumina spacers which we use to insulate the sensors from the plugs.

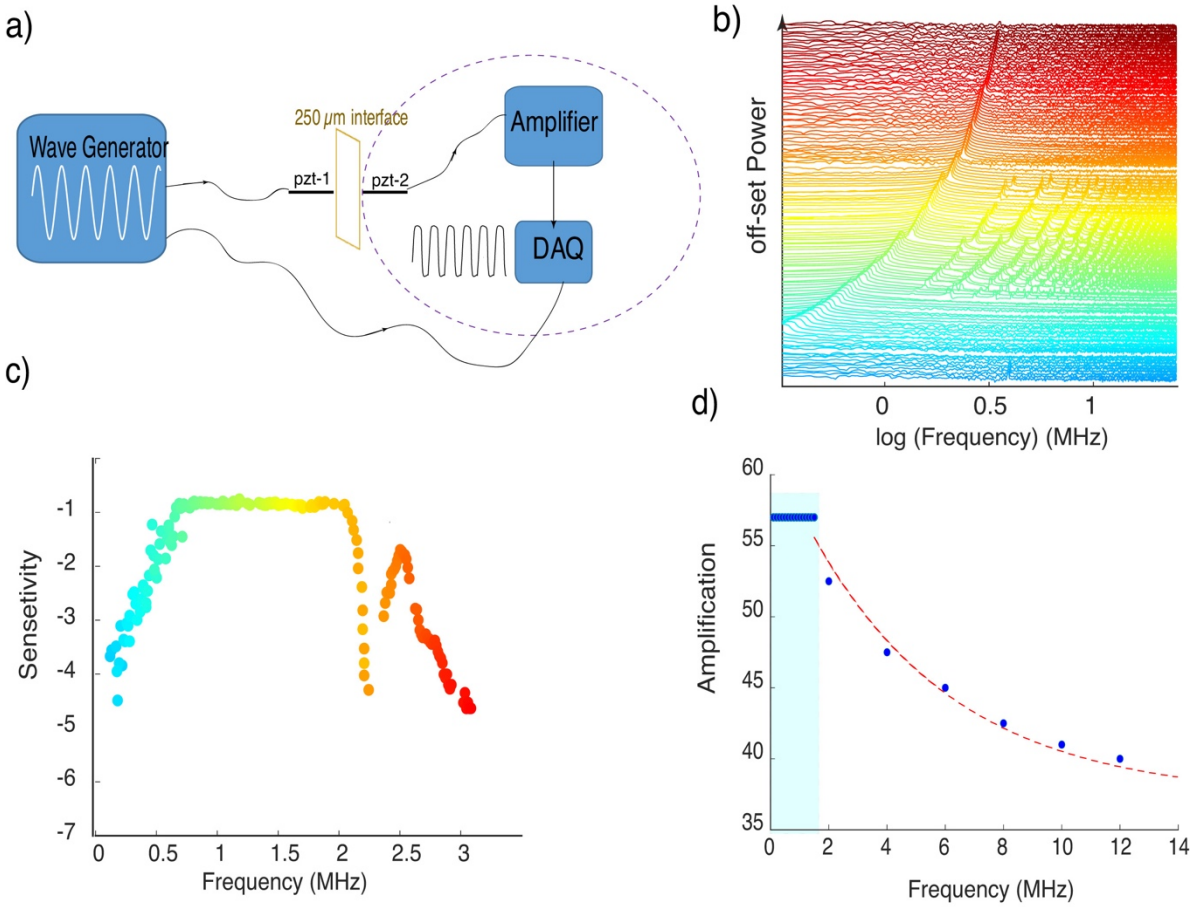

Figure 8| Relative response of a sensor to an identical sensor emitting sweeping sin waves from 5 kHz to 10MHz. (a) We used a thin interface of mica (~50 to 250 μm) to avoid direct contact of the face-to-face sensors. (b) response of the receiver (pzt-2) to a range of frequencies generated as sin waves. We plotted off-set power spectrum of the natural logarithmic scale of the response frequency from 80kHz to ~3MHz . The spectrum for each signal is normalized to the maximum of the power. (c) Sensitivity of the sensor shows that the response of the sensor is almost flat to generated waves in the range of 600kHz to 2MHz and a clear resonance peak around 2.5Mhz occurs. The sensors are sensitive from 80kHz to 3MHz for the pulser signal of a 5V peak to peak amplitude. (d) Response of the amplifier to generated sin waves with amplitudes 2-20mV, frequencies changing from 100 kHz to 15 MHz and duration of at least 1μs. The amplifier has an approximately flat amplification response (~57dB) for frequencies below 1.5 MHz. Amplification of signals with higher frequencies decreases exponentially while the amplifier gate is fixed at 60dB.

5.3 Physical Parts of the Ultrasound Probe Systems and Data Acquisition

Figure 9 shows the diagram of all units which we used for our 4 channel ultrasound recording system. The DAQ system in our set-up records in trigger mode in which a threshold level is used to capture waveforms for each channel with a set length. The most sensitive but least noisy sensor(s) is selected as the "master" sensor which triggers recording in all channels (Cecchi software by Itasca). The maximum rate of recording in our system is 800 waveforms per second

for 4 channels with a waveform length of 200 µs and a resolution of 12 bits (using USB 2.0 High Speed: 480 Mbit/s). For our tests, we used waveforms with a length of 80 to 400 µs, 12bit resolution and a sampling rate of 50MS/s.

The illustrated circuit includes a pulser unit (up to 900V, broad frequency range from DC up to 30MHz - JSR Ultrasonics DPR300 Pulser/Receivers) controlled by a function generator (Agillant 33522A) which feeds into the top piezoelectric sensor for active ultrasound experiments. All amplifiers are supplied with a DC power supplier (Korad KA3005P).

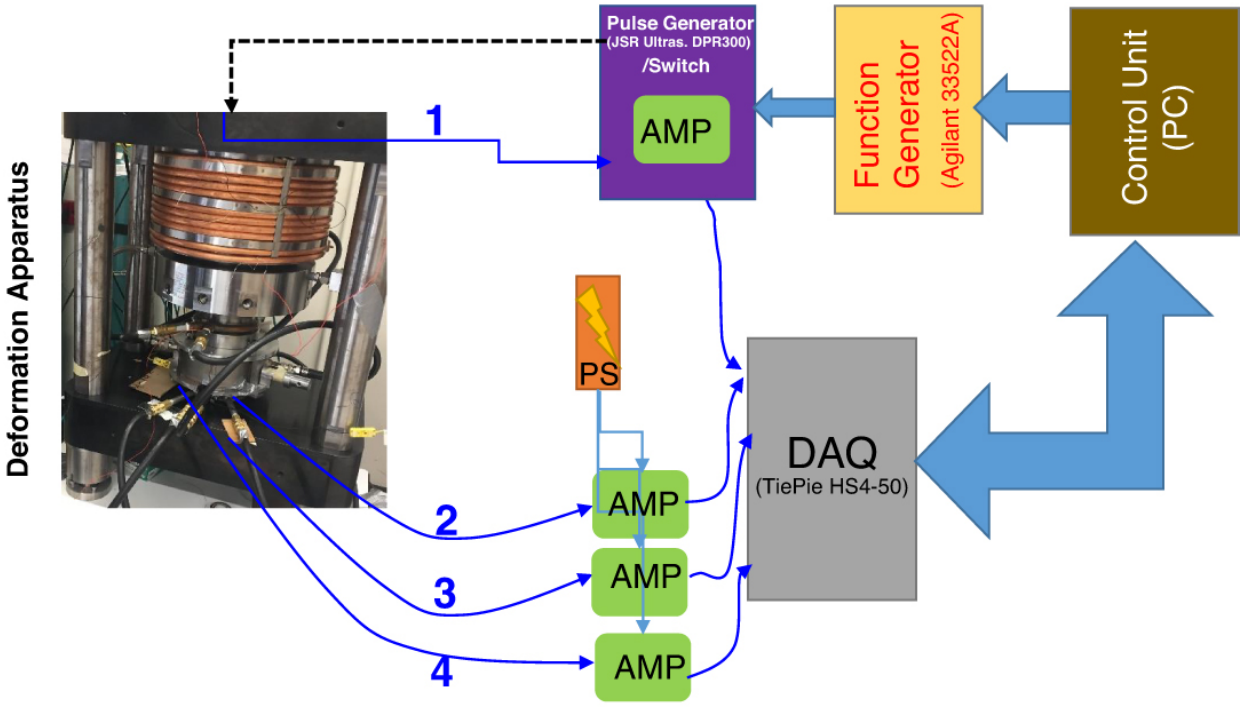

Figure 9. Diagram of the physical parts of the ultrasound probe system for 4 independent piezoelectric sensors. The amplifiers (AMP) are powered by an AC-DC power supplier (PS). Pulse generator and Data acquisition (DAQ) system are controlled with a control unit using a PC. All units are grounded with the rig as the reference ground. The pulse generator allows generating impulsive pulses with duration up to 150ns and power of 900V. The interval of pulsing is defined with a wave function generator.

6 EMI effects and techniques for reducing noise in the apparatus

EMI is one of the principal plagues of AE recording; noise spikes in the system can make trigger-based recording of AEs impossible. One of the classic characteristics of EMI noise is its highly unpredictable behavior. EMI noises are generally lower at night than during the day. In this section we discuss our workflow and methods we used to decrease electromagnetic interference noises at MIT down to the levels which allow us to record at 60dB amplification with a background noise of ≈90mV at +/- 2V full scale.

6.1 Heating-Induced EMI

The most common SCR operation mode is phase angle firing, where the AC wave is cut at a non-zero voltage. This is accompanied by high amplitude spikes. An SCR conducts load current in one direction and is a class of thyristor family (*Mathur and Varma, 2002*). Considering an AC circuit, during the positive half cycle of an AC sinusoidal waveform, the thyristor is biased and can be triggered by a pulse ("gate signal"). During the negative half cycle, the thyristor is reverse biased and cannot conduct power. Therefore, employing a gate signal at the appropriate time and during the positive half of an AC waveform, the thyristor is triggered to conduct power (i.e., "phase control"). If the thyristor is triggered at the beginning of the half-cycle (phase angle = 0^o), the power will continue for the full positive cycle of the AC waveform. If the gate trigger pulse moves along the half cycle ($\theta = 0^o$ to 90^o), the supplied power is decreases. During gate triggering at $\theta > 0^o$ and $< 90^o$, the AC waveform is chopped off at non-zero current which is accompanied by induced electromagnetic noises in the range of kHz to GHz. An effective way to reduce these induced electromagnetic noises is to use fast zero (instant-on) switching which turns the thyristor on immediately after the application of the gate pulse-triggering signal at zero current. This random-fire switching is used in resistive applications such as lamp dimming and applications that require the load only to be energized for a small portion of the AC cycle. Using in-line filters within the electrical circuit of SCR such as resistor–capacitor circuit (i.e., RC network) and control box also further reduce the induced electronic noises (*Horowitz and Hill,1989*). We further install ferrite beads on the heating system cables connected to the secondary circuit of the step down transformer (see Figure 1). A detailed electrical drawing of our heating system is available by download from *Ghaffari and Pec 2020.*

6.2 Grounding

The second step in decreasing the noise level is to ground the piezoelectric elements (or amplifiers) properly with the body of the rig. The proper grounding of acquisition systems as well as employed PCs for various parts of the rig reduce noise significantly. We connect the body of the amplifiers to the body of the deformation apparatus to achieve optimum grounding. Another step which helps to minimize the induced noises was to use short sensors and short BNC cables carrying unamplified signals. When shortening the needle sensors, the connecting pin (main

signal carrier) is carefully cut and re-connected to micro-BNC cables while the connection part is sprayed with several layers of EMI and dielectric sprays. Isolation transformers (TripLite 1800HG) are used to isolate any electrical equipment connected to the deformation apparatus (DAQ computer, AC motors running the syringe pumps). The addition of the isolation transformers to the power supply of the two syringe pumps (see Section 3.1.1) has significantly decreased the background noise level in our case. Prior to the main experiment, we use an empty furnace which is pressed on the WC plug and makes an electrical circuit with the upper σ_1 piston. We examine each sensor's EMI resistance while we increase the temperature of the assembly up to ~80˚ to 120˚C. By using the combination of the above methods, we decreased the noise level of sensors plus amplifiers to ~90mV at 60dB amplification of raw signals.

7 Demonstration of the Experimental Capabilities

We briefly discuss our preliminary results on deformation of quartzite rock samples deformed at $P = 0.5 – 1$ GPa and $T = 375$˚C with 2 to 4 piezoelectric sensors to demonstrate the experimental capabilities of our system. Extended results at higher temperatures and confining pressures will be reported elsewhere. In the following experiments we have decreased the noise level to an *ambient* noise level in the ultrasound recording system such that with 60dB amplification the triggering noise level is set at 90mV using a +/- 2V full scale. Alumina spacers with a thickness of ~600 μm are used to insulate the sensor tips from the WC plugs. Prior to pressurization, we examine sensitivity of the sensors and their coupling with the WC plug using a ball drop experiment, crackling pencil lead (0.7 mm clay-graphite leads), capillary glasses (1 mm thickness of hollow glasses) and spaghetti (1.3 mm thickness) in back of the base plate as each source emits waves in a different frequency range.

7.1 Patterns of Damage Accumulation

During each experiment, the recorded AEs can be subdivided into three stages (**Fig.10**): Stage 1 occurs during pressurization and heating (i.e., pre-deformation) where the confining pressure and temperature is increased up to the desired value. Most of the AEs are due to mechanical and thermal cracking of solid media (solidified salt) and furnace including graphite and insulator pyrophyllite shells, some cracking in the sample itself is also possible. The number of recorded AEs depends on the sensitivity of the sensors and the quality of assembly as well as porosity of the solidified salts, this phase usually exceeds 1000 accumulative AEs events (**Fig.10**).

Generally speaking, the number of events decreases as the P and T increases. The waveforms are dominantly long-duration and quite similar to low confinement experiments on brittle materials **(Fig. 10)**.

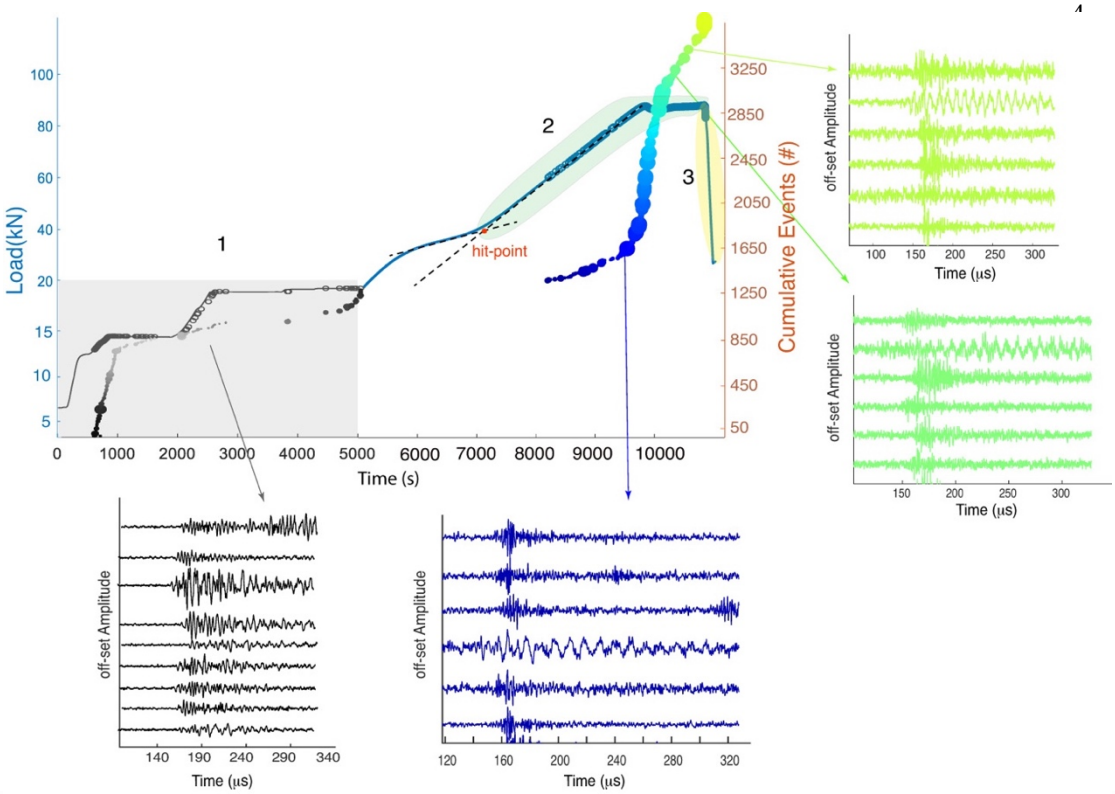

Figure 10| Example of accumulative acoustic emission hits during pressurization (1), deformation (2) and quenching (3) stages of an experiment performed at Pc = 0.5 GPa and T = 375˚C with a 4-sensor array. The size of circles are proportional to the maximum absolute amplitude of signal, color coding indicates elapsed time. We also show some typical waveforms from the stage 1, 2 and 3.

Stage 2 is the main deformation phase where the σ_1 piston is driven into the assembly at a constant displacement rate yielding a "run-in" curve. Initial events in this phase prior to "hit point" are rare and of small magnitude (maximum amplitude, $|A_{max}|$<200mV). We speculate that the origin of such events is mostly due to driving of the σ_1 WC piston into the lead and compaction of any surviving void spaces in the assembly and sample. After the hit-point, AE activity increases and large amplitude AEs become common. The AE vs. time curve shows a sigmoidal pattern; initially at low differential stresses the AE rate is slow, the AE rate increases significantly shortly before the sample reached peak strength, and then decreases again during steady state flow as illustrated in Figure 10. The AEs clearly correlate with the mechanical data.

We end the paper with an example of source location. The simplest localization method is to use two sensors above and below the sample and assume an essentially 1-D problem (**Fig.11**). Knowing the velocity of each component of the assembly and considering that the top sensor is mobile, i.e., its motion correlates with the measured motion of the σ_1 piston and deformation of the assembly while the bottom sensor is fixed, we can estimate the location of the AE source as demonstrated in Figure 11.

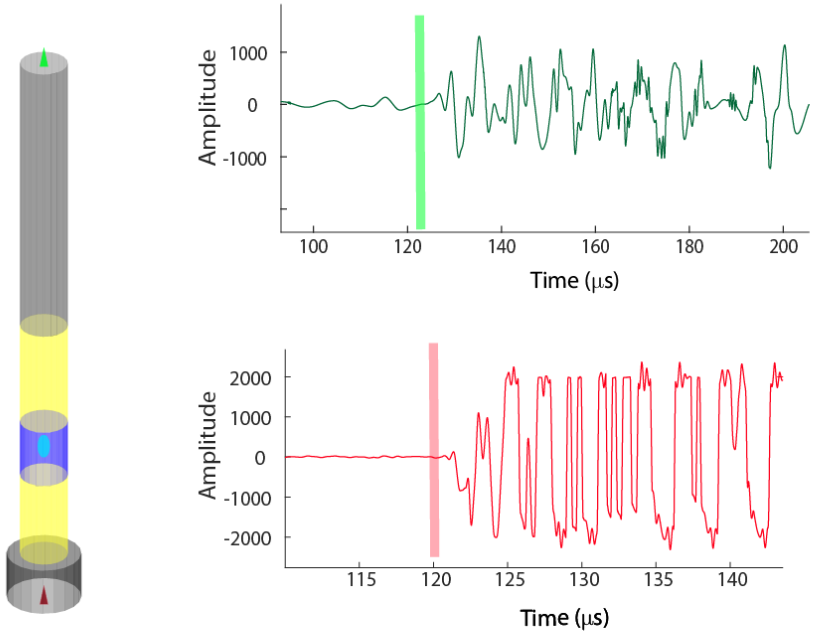

Figure 11 AE location in 1-D. The sensor locations are shown as colored triangles. Located events are shown as colored circles, the maximum amplitude of the event scales with the circle size. a) Using two piezoelectric sensors one can define the localization of events in the z-direction. An example of the recorded events where the source location occurs within the sample (blue-green circles).

8 Conclusion and future work

In this paper, we described the detailed design and implementation of an ultrasound probe array system into a high-pressure and high-temperature deformation apparatus. Considerations of selection of piezoelectric elements, amplifiers, DAQ system, cooling system and mechanical stability of the apparatus were also described. We discuss our strategies for decreasing EMI noises which pose a major problem for recording AEs at *HP-HT* conditions. We provided analysis on the relative response of the miniature piezoelectric sensors and our DAQ system, we established that our sensors are able to reflect correctly the source duration and frequency of the sources if they are in the frequency range of sensors and amplifiers (600 kHz – 2.5 MHz). At last, we

illustrated the capability of our system with up to 4 piezoelectric sensors to record hundreds of weak events at *HP-HT* conditions and locate them within the sample with acceptable accuracy at pressures of up to 1 GPa and temperatures of up to 375˚C. The temperature range can be easily extended up to ≈ 1200˚C by using alumina or zirconia spacers of appropriate length. Higher pressures are also in principle achievable; however, we have not tested this capability yet. There is a possibility to extend the design to incorporate more piezoelectric sensors. One option is to fabricate smaller sensors (as small as 0.3 mm diameter) which would allow placement of more sensors in the base plate . Another possibility – at least for certain pressures and temperatures – is to use high temperature piezoelectric crystals mounted directly on the sample jacket. Exploring such avenues would allow for a more complete spatial coverage of the deforming sample moment tensor analysis of a given recorded AE. Furthermore, the employed sensors can be calibrated using established methods such as ball drop experiments or laser interference methods to calibrate the sensor for a certain mechanical parameter such as velocity or acceleration. Adding S-sensors to the array and conducting active ultrasound experiments will allow for elastic moduli calculation and detecting changes in wave speed with deformation.

Acknowledgements:

The authors would like to thank Ulrich Mok (MIT), William Flynn (Itasca Co.), Valdemar Krzyzanowski (NDtxducer Co.), Martin Lilly (Dynasen Inc.), Eric Burdette (Brown University), and Alexandre Schubnel (ENS Paris) for useful suggestions and feedbacks in integration of different parts of the described system. Andrew Gallant and Andrew Ryan at the MIT machine shop for designing and manufacturing various pieces that enabled this study. NSF funding through the Instrumentation & Facilities grant 1836304 for the development of this system as well as funding for lab tech support grant 1833478 is gratefully acknowledged. CAD drawings and MATLAB codes described can be downloaded from *Ghaffari and Pec 2020*. Reviews from two anonymous reviewers helped improve the manuscript and are gratefully acknowledged.

References

Agarwal, A. B. L., Frederick, J. R., & Felbeck, D. K. (1970). Detection of plastic microstrain in aluminum by acoustic emission. *Metallurgical Transactions*, *1*(4), 1069.

Aki, K., & Richards, P. G. (2002). *Quantitative seismology*.

Précigout, J., Stünitz, H., Pinquier, Y., Champallier, R., & Schubnel, A. (2018). High-pressure, High-temperature Deformation Experiment Using the New Generation Griggs-type Apparatus. *JoVE*, (134), e56841. https://doi.org/doi:10.3791/56841

Bak, P., & Tang, C. (1989). Earthquakes as a self-organized critical phenomenon. *Journal of Geophysical Research: Solid Earth*, *94*(B11), 15635–15637.

Bass, J. D., & Zhang, J. S. (2015). 2.12 - Theory and Practice: Techniques for Measuring High-P–T Elasticity A2 - Schubert, Gerald BT - Treatise on Geophysics (Second Edition) (pp. 293–312). Oxford: Elsevier. https://doi.org/http://dx.doi.org/10.1016/B978-0-444-53802-4.00037-3

Benson, P. M., Vinciguerra, S., Meredith, P. G., & Young, R. P. (2008). Laboratory simulation of volcano seismicity. *Science*, *322*(5899), 249–252.

Birch, F. (1939). The variation of seismic velocities within a simplified earth model, in accordance with the theory of finite strain. *Bulletin of the Seismological Society of America*, *29*(3), 463–479.

Blacic, J. D., & Hagman, R. L. (1977). Wide-band optical–mechanical system for measuring acoustic emissions at high temperature and pressure. *Review of Scientific Instruments*, *48*(7), 729–732.

Borch, R. S., & Green, H. W. (1989). Deformation of peridotite at high pressure in a new molten salt cell: Comparison of traditional and homologous temperature treatments. *Physics of the Earth and Planetary Interiors*, *55*(3–4), 269–276.

Brekhovskikh, L. (2012). *Waves in layered media* (Vol. 16). Elsevier.

Bridgman, P. W., & Bridgman, P. W. (1931). The physics of high pressure.

Burnley, P. C., & Getting, I. C. (2012). Creating a high temperature environment at high pressure in a gas piston cylinder apparatus. *Review of Scientific Instruments*, *83*(1), 14501.

Burnley, P. C., & Zhang, D. (2008). Interpreting in situ x-ray diffraction data from high pressure deformation experiments using elastic--plastic self-consistent models: an example using quartz. *Journal of Physics: Condensed Matter*, *20*, 285201.

Chantel, J., Manthilake, G., Andrault, D., Novella, D., Yu, T., & Wang, Y. (2016). Experimental evidence supports mantle partial melting in the asthenosphere. *Science Advances*, *2*(5), e1600246.

Dobson, D. P., Meredith, P. G., & Boon, S. A. (2002). Simulation of subduction zone seismicity by dehydration of serpentine. *Science*, *298*(5597), 1407–1410.

French, M. E., Hirth, G., & Okazaki, K. (2019). Fracture-induced pore fluid pressure weakening and dehydration of serpentinite. *Tectonophysics*, *767*, 228168.

Gasc, J., Schubnel, A., Brunet, F., Guillon, S., Mueller, H.-J., & Lathe, C. (2011). Simultaneous acoustic emissions monitoring and synchrotron X-ray diffraction at high pressure and temperature: Calibration and application to serpentinite dehydration. *Physics of the Earth and Planetary Interiors*, *189*(3–4), 121–133.

Ghaffari, H. O., Griffith, W. A., & Pec, M. (2019). Solitonic State in Microscopic Dynamic Failures. *Scientific Reports*, *9*(1), 1967. https://doi.org/10.1038/s41598-018-38037-w

Ghaffari, H. O., Nasseri, M. H. B., & Young, R. P. (2014). Faulting of rocks in a three-dimensional stress field by micro-anticracks. *Scientific Reports*, *4*, 5011.

Ghaffari, H. O., Pec, M., (2020) An ultrasound probe array for a high-pressure, high-temperature solid medium deformation apparatus: CAD drawings and MATLAB codes. *Zenodo.org, doi: 10.5281/zenodo.3634975*

Ghaffari, H. O., & Young, R. P. (2013). Acoustic-friction networks and the evolution of precursor rupture fronts in laboratory earthquakes. *Scientific Reports*, *3*, 1799.

Gleason, G. C., & Tullis, J. (1995). A flow law for dislocation creep of quartz aggregates determined with the molten salt cell. *Tectonophysics*, *247*(1–4), 1–23.

Glover, P. W. J., Baud, P., Darot, M., Meredith, Pg., Boon, S. A., LeRavalec, M., et al. (1995). α/β phase transition in quartz monitored using acoustic emissions. *Geophysical Journal International*, *120*(3), 775–782.

Green, H. W., Scholz, C. H., Tingle, T. N., Young, T. E., & Koczynski, T. A. (1992). Acoustic emissions produced by anticrack faulting during the olivine→ spinel transformation. *Geophysical Research Letters*, *19*(8), 789–792.

Griggs, D. (1967). Hydrolytic weakening of quartz and other silicates. *Geophysical Journal International*, *14*(1–4), 19–31.

Guéguen, Y., & Schubnel, A. (2003). Elastic wave velocities and permeability of cracked rocks. *Tectonophysics*, *370*(1–4), 163–176.

Gutenberg, B., & Richter, C. F. (1955). Magnitude and energy of earthquakes. *Nature*, *176*(4486), 795.

Heilbronner, R., & Tullis, J. (2006). Evolution of c axis pole figures and grain size during dynamic recrystallization: Results from experimentally sheared quartzite. *Journal of Geophysical Research*, *111*.

Hirth, G., & Tullis, J. (1994). The brittle-plastic transition in experimentally deformed quartz aggregates. *Journal of Geophysical Research-Solid Earth*, *99*(B6).

Holyoke, C. W., & Kronenberg, A. K. (2010). Accurate differential stress measurement using the molten salt cell and solid salt assemblies in the Griggs apparatus with applications to strength, piezometers and rheology. *Tectonophysics*, 1–15. https://doi.org/10.1016/j.tecto.2010.08.001

Holyoke, C. W., Kronenberg, A. K., Newman, J., & Ulrich, C. (2014). Rheology of magnesite. *Journal of Geophysical Research: Solid Earth*, *119*(8), 6534–6557.

Horowitz, P., & Hill, W. (1989). *The art of electronics*. Cambridge Univ. Press.

Incel, S., Hilairet, N., Labrousse, L., John, T., Deldicque, D., Ferrand, T., et al. (2017). Laboratory earthquakes triggered during eclogitization of lawsonite-bearing blueschist. *Earth and Planetary Science Letters*, *459*, 320–331.

Kern, H. (1982). Elastic-wave velocity in crustal and mantle rocks at high pressure and temperature: the role of the high-low quartz transition and of dehydration reactions. *Physics of the Earth and Planetary Interiors*, *29*(1), 12–23.

Kohlbrecher, J., Bollhalder, A., Vavrin, R., & Meier, G. (2007). A high pressure cell for small angle neutron scattering up to 500 MPa in combination with light scattering to investigate liquid samples. *Review of Scientific Instruments*, *78*(12), 125101.

Li, B., & Liebermann, R. C. (2014). Study of the Earth's interior using measurements of sound velocities in minerals by ultrasonic interferometry. *Physics of the Earth and Planetary Interiors*, *233*, 135–153.

Lockner, D. (1993). The role of acoustic emission in the study of rock fracture. In *International Journal of Rock Mechanics and Mining Sciences & Geomechanics Abstracts* (Vol. 30, pp. 883–899). Elsevier.

Mathur, R. M., & Varma, R. K. (2002). *Thyristor-based FACTS controllers for electrical transmission systems*. John Wiley & Sons.

McLaskey, G. C., & Kilgore, B. D. (2013). Foreshocks during the nucleation of stick-slip instability. *Journal of Geophysical Research: Solid Earth*, *118*(6), 2982–2997.

Okazaki, K., & Hirth, G. (2016). Dehydration of lawsonite could directly trigger earthquakes in subducting oceanic crust. *Nature*, *530*(7588), 81–84.

Passelègue, F. X., Schubnel, A., Nielsen, S., Bhat, H. S., & Madariaga, R. (2013). From sub-Rayleigh to supershear ruptures during stick-slip experiments on crustal rocks. *Science*, *340*(6137), 1208–1211.

Pec, M., Stünitz, H., & Heilbronner, R. (2012). Semi-brittle deformation of granitoid gouges in shear experiments at elevated pressures and temperatures. *Journal of Structural Geology*, *38*(0), 200–221. https://doi.org/10.1016/j.jsg.2011.09.001

Pec, M., Stünitz, H., Heilbronner, R., & Drury, M. (2016). Semi-brittle flow of granitoid fault rocks in experiments. *Journal of Geophysical Research: Solid Earth*, *121*(3), 1677–1705. https://doi.org/10.1002/2015JB012513

Pec, M., Stünitz, H., Heilbronner, R., Drury, M., & de Capitani, C. (2012). Origin of pseudotachylites in slow creep experiments. *Earth and Planetary Science Letters*, *355–356*(0), 299–310. https://doi.org/10.1016/j.epsl.2012.09.004

Ronde, A. A. De, Stünitz, H., Tullis, J., & Heilbronner, R. (2005). Reaction-induced weakening of plagioclase--olivine composites. *Tectonophysics*, *409*(1–4), 85–106.

Rouet-Leduc, B., Hulbert, C., Lubbers, N., Barros, K., Humphreys, C. J., & Johnson, P. A. (2017). Machine learning predicts laboratory earthquakes. *Geophysical Research Letters*, *44*(18), 9276–9282.

Rybacki, E., Renner, J., Konrad, K., Harbott, W., Rummel, F., & Stöckhert, B. (1998). A servohydraulically-controlled deformation apparatus for rock deformation under conditions of ultra-high pressure metamorphism. *Pure and Applied Geophysics*, *152*(3), 579–606.

Schubnel, A., Champallier, R., Precigout, J., Pinquier, Y., Ferrand, T. P., Incel, S., et al. (2015). GRAAL-Griggs-type Apparatus equipped with Acoustics in the Laboratory: a new instrument to explore the rheology of rocks at high pressure. In *AGU Fall Meeting Abstracts*.

Schubnel, A., Brunet, F., Hilairet, N., Gasc, J., Wang, Y., & Green, H. W. (2013). Deep-Focus Earthquake Analogs Recorded at High Pressure and Temperature in the Laboratory. *Science*, *341*(6152), 1377 LP – 1380. https://doi.org/10.1126/science.1240206

Stewart, E. D., Holyoke III, C. W., & Kronenberg, A. K. (2013). High pressure deformation experiments using solid confining media and Griggs piston-cylinder methods: Appraisal of stress and deformation in talc assemblies. *Tectonophysics*, *588*, 171–178.

Tarantola, A., Diamond, L., Stünitz, H., Thust, A., & Pec, M. (2012). Modification of fluid inclusions in quartz by deviatoric stress. III: Influence of principal stresses on inclusion density and orientation. *Contributions to Mineralogy and Petrology*, *164*(3), 537–550. Retrieved from http://dx.doi.org/10.1007/s00410-012-0749-1

Thompson, B. D., Young, R. P., & Lockner, D. A. (2009). Premonitory acoustic emissions and stick-slip in natural and smooth-faulted Westerly granite. *Journal of Geophysical Research: Solid Earth*, *114*(B2).

Tingle, T. N., Green, H. W., Young, T. E., & Koczynski, T. A. (1993). Improvements to Griggs-type apparatus for mechanical testing at high pressures and temperatures. *Pure and Applied Geophysics*, *141*(2–4), 523–543.

Tullis, T. E., & Tullis, J. (1986). Experimental rock deformation techniques. In *Mineral and rock deformation: Laboratory studies* (Vol. 36, pp. 297–324). American Geophysical Union Washington, DC.

Vinogradov, A., Vasilev, E., Seleznev, M., Máthis, K., Orlov, D., & Merson, D. (2016). On the limits of acoustic emission detectability for twinning. *Materials Letters*, *183*, 417–419.

Vinogradov, A. (2010). On shear band velocity and the detectability of acoustic emission in metallic glasses. *Scripta Materialia*, *63*(1), 89–92.

Wadley, H. N. G., & Mehrabian, R. (1984). Acoustic emission for materials processing: a review. *Materials Science and Engineering*, *65*(2), 245–263.

Wang, Y., Durham, W. B., Getting, I. C., & Weidner, D. J. (2003). The deformation-DIA: A new apparatus for high temperature triaxial deformation to pressures up to 15 GPa. *Review of Scientific Instruments*, *74*(6), 3002–3011.

Wang, Y., Zhu, L., Shi, F., Schubnel, A., Hilairet, N., Yu, T., et al. (2017). A laboratory nanoseismological study on deep-focus earthquake micromechanics. *Science Advances*, *3*(7), e1601896.

Weiss, J., & Marsan, D. (2003). Three-dimensional mapping of dislocation avalanches: clustering and space/time coupling. *Science*, *299*(5603), 89–92.

Ziola, S. M., & Gorman, M. R. (1991). Source location in thin plates using cross-correlation. *The Journal of the Acoustical Society of America*, *90*(5), 2551–2556.